RSC Advances

PAPER

View Article Online
View Journal | View Issue

Cite this: *RSC Adv.*, 2025, **15**, 11283

Manganese-based nanoparticles plus gambogic acid targeted hypoxic tumor microenvironment by enhancing ROS generation and provided antitumor treatment and improved immunotherapy†

Zixin Liang, ‡[a] Xinyi Xu,[a] Ning Wang,[a] Xintao He,[b] Xingzhi Han,[c] Liuqi Sang,[d] Jing Hu*[a] and Xiaoping Qian*[a]

Colorectal cancer (CRC) remains a major global health challenge, particularly in advanced stages where drug resistance leads to high recurrence rates and poor survival outcomes. This study investigates a novel therapeutic approach combining gambogic acid (GA) with manganese dioxide (MnO_2) nanoparticles (MBG NPs) to enhance anti-tumor efficacy in the acidic and hypoxic tumor microenvironment (TME). The development of MBG NPs involved conjugating MnO_2 nanosheets with bovine serum albumin (BSA) for effective GA encapsulation, optimizing the delivery of both components. We explored the potential of Mn^{2+} ions released from MnO_2 to synergize with GA to alleviate tumor hypoxia and modulate the TME, thereby improving immune response. *In vitro* assays demonstrated significant cytotoxicity of MBG NPs against mouse colon cancer cells (CT26 cells), with enhanced apoptosis and elevated reactive oxygen species (ROS) levels. *In vivo* studies using BALB/c mice showed that treatment with MBG NPs significantly reduced tumor volumes and improved survival rates compared to controls. Additionally, MBG NPs combined with programmed death-1 inhibitor (aPD-1) further augmented therapeutic effects. Histological analyses confirmed tumor necrosis and changes in TME composition, indicating the potential of this synergistic strategy to overcome drug resistance in microsatellite stable (MSS) CRC, inhibit tumor growth and benefit patient survival. These findings highlight the promising application of nanoparticle-based platforms in enhancing immunotherapy outcomes for advanced colorectal cancer.

Received 4th December 2024
Accepted 17th March 2025

DOI: 10.1039/d4ra08547g

rsc.li/rsc-advances

1. Introduction

Colorectal cancer (CRC) is the third most common cancer worldwide, with high incidence and mortality rates. Although the prevalence of early cancer screening and improved treatment options have increased the five-year survival rate for patients, the issue of drug resistance often leads to tumor recurrence, with a mere 14% five-year survival rate in advanced CRC patients.[1] Thus, it is crucial to explore new treatment strategies for advanced CRC and to improve drug resistance. Immune-checkpoint inhibitors (ICIs) constitute a major research direction in immunotherapy, offering hope for patients with advanced CRC. However, most patients with proficient DNA mismatch repair (pMMR) or microsatellite stable (MSS) CRC show limited responses to ICIs.[2] In-depth studies of molecular mechanisms indicate that the tumor microenvironment (TME), characterized by low pH, hypoxia, and high levels of oxidative stress, is a major reason for poor responses to ICIs therapy. The acidic and hypoxic TME hinders the infiltration and activity of immune cells, resulting in T cell exhaustion and tumor immune evasion.[3] Therefore, the urgent challenge is to combine immunotherapy with other drugs, to overcome immune resistance induced by the TME and reverse ICIs resistance.

Gambogic acid (GA), derived from the traditional Chinese medicine gamboge, has been found to curb the progression of various malignancies through multiple mechanisms, including the induction of autophagy, inhibition of tumor metastasis, and anti-angiogenesis.[4] Additionally, recent studies suggest that GA can induce apoptosis in cancer cells through reactive oxygen species (ROS) signaling, with elevated ROS levels associated with GA-mediated cell death.[5] Our team has successfully

[a]*Department of Oncology, Nanjing Drum Tower Hospital Clinical College of Nanjing University of Chinese Medicine, Nanjing, China. E-mail: xiaopingqian@nju.edu.cn; doctorhujing@163.com*

[b]*Department of Pathology, Nanjing Drum Tower Hospital Clinical College of Nanjing University of Chinese Medicine, Nanjing, China*

[c]*Nanjing Drum Tower Hospital, Affiliated Hospital of Medical School, Nanjing University, Nanjing, China*

[d]*Nanjing Drum Tower Hospital Clinical College of Xuzhou Medical University, Nanjing, China*

† Electronic supplementary information (ESI) available. See DOI: https://doi.org/10.1039/d4ra08547g

‡ These authors contributed equally to this work.

developed nanoparticle-based drug delivery systems to effectively encapsulate GA which overcome the disadvantages of GA such as poor water solubility,[6] and we found that GA can promote dendritic cells (DC) maturation.[7] But the mechanism behind its potential enhancement of programmed death-1 inhibitor (aPD-1) is still unclear. In this study, we also aim to investigate this further.

In recent years, gold nanostructures and two-dimensional nanomaterials have garnered significant attention as drug carriers for combined cancer therapies.[8] Among reported nanoparticle-based drug delivery systems, MnO_2 nanostructures serve as a unique TME-responsive carrier, offering several distinct advantages: first, MnO_2 can decompose H_2O_2 present in the TME into O_2.[9] Second, MnO_2 can react with H^+ or glutathione (GSH) in the TME to produce Mn^{2+} ions, targeting the tumor's acidic microenvironment.[10,11] Furthermore, Mn^{2+} is a valuable T1 contrast agent, and many studies have utilized this property for magnetic resonance imaging (MRI) to continuously monitor drug kinetics *in vivo*.[12,13] In conclusion, MnO_2 nanostructures have been found to enhance various cancer therapies.[14] Bovine serum albumin (BSA) possesses high drug loading capacity and effectively extends drug half-lives,[15] making it a beneficial candidate for developing nanoparticle-based drugs. Nab-paclitaxel (Abraxane®), a formulation for delivering paclitaxel, has been widely used and approved by the Food and Drug Administration (FDA).[16]

During the sonication process, the collapse of microbubbles generates high temperature and pressure, which facilitates the incorporation of BSA into the layered MnO_2.[17] Compared to traditional MnO_2 nanoparticles (MnO_2 NPs), protein-templated MnO_2 NPs exhibited better biocompatibility.[18] So, we synthesized MnO_2-BSA (MB NPs) by conjugating MnO_2 nanostructures with BSA. Combining Mn^{2+} ions with GA can synergistically improve the hypoxic and acidic TME. It will enhance tumor killing and augmenting anti-tumor immune responses. Thus, we further load GA into MB NPs to generate MnO_2-BSA-GA (MBG NPs). The MnO_2 in the material can react in an acidic environment to release Mn^{2+} ions. This material can simultaneously increase the concentration of Mn^{2+} ions and GA at the tumor site for optimal anti-tumor effects. They both against and regular the acidic hypoxic TME of MSS CRC. Compared with other existing GA NPs, we successfully developed simple to fabricate MBG NPs that enable cells to produce ROS and improve hypoxic acidic TEM, providing a new possibility for clinical translation of GA, which will provide a new strategy for MSS CRC.[13,19]

So, comprehensive *in vitro* and *in vivo* evaluations were performed. Our research focuses on determining how to target the tumor site, increase the concentration of Mn^{2+} ions and GA within the tumor and maintain biosafety and explore the reasons why GA enhances the efficacy of aPD-1.

2. Results and discussion

2.1 Preparation and characterization of MBG NPs

We prepared MBG NPs in two steps (Fig. 1A): first, MnO_2 nanostructures were obtained by ultrasonication of BSA solution. Subsequently, GA was loaded onto the carrier using Nab™ technology. Compared to a simple BSA formulation, the addition of MnO_2 transformed the drug from a yellow clear liquid to a brownish-yellow clear liquid. MnO_2 nanostructures can degrade H_2O_2 present in TME into O_2, alleviating tumor hypoxia.[9] Additionally, they can react with H^+ or GSH in the TME, targeting the acidic microenvironment and acting as a strong adjuvant.[10] So, we hypothesized that combining the three components would produce a "1 + 1 + 1 > 3" effect. The morphology of GA, BG NPs and MBG NPs were observed by TEM, the observed images were shown in Fig. 2A. It was observed that GA samples appeared in spherical form and adsorbed GA through BSA and MnO_2. Elemental analysis was then performed by using EDX mappings. The analysis results showed that, compared with GA and BG NPs, there was significant Mn enrichment in MBG NPs, confirming the structural characteristics observed by TEM and the successful construction of MBG NPs. DLS measurement indicated that the average size of MnO_2, MB, BG and MBG NPs were approximately 84.86 ± 0.15 nm, 106.1 ± 0.35 nm, 181.1 ± 0.26 nm and 157 ± 0.92 nm(Fig. 2C). The zeta potential of MnO_2 was −37.8 ± 0.14 mV, after modification with BSA, the zeta potential of MB NPs changed to −16 ± 0.15 mV, and the potential of the final product MBG NPs was −14.47 ± 0.29 mV (Fig. 2D). These changes in particle size reconfirm the successful loading of GA.[20–22] Additionally, we evaluated the long-term stability of the NPs; dispersing them in PBS for one week showed no significant changes in particle size or polymer dispersity index (PDI), indicating excellent stability and ensuring the feasibility of subsequent experiments (Fig. 2E). To enhance GA encapsulation

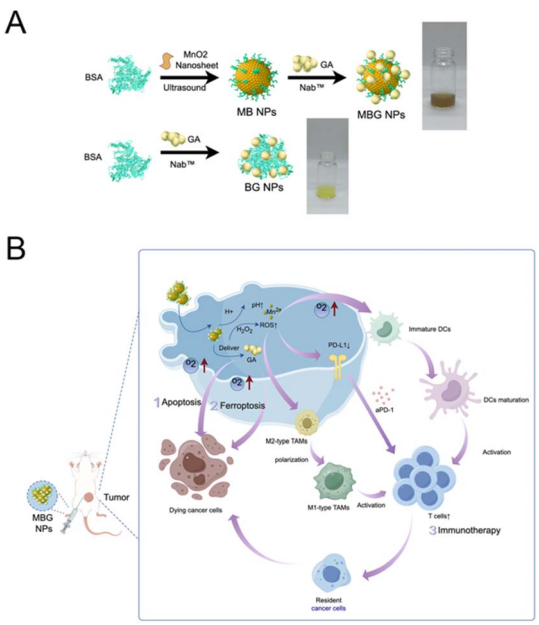

Fig. 1 Overall scheme for the design and development of NPs. (A) Schematic diagram of the synthesis process of MBG and BG, involving the simple mixing of MnO_2 and BSA solutions. (B) Subcutaneous injection of MBG NPs can inhibit primary tumor growth and effectively enhance oxygen delivery, leading to increased ROS and reversal of the hypoxic tumor microenvironment, which is beneficial for anti-tumor immunity by modulating immune cell composition to overcome aPD-1 resistance.

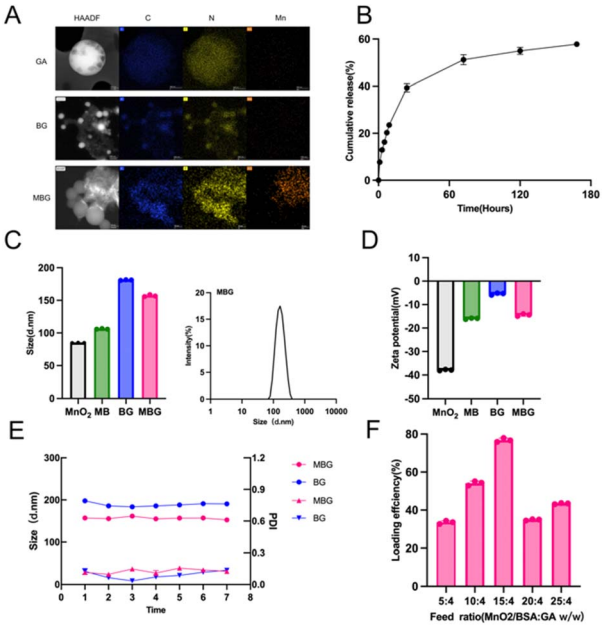

Fig. 2 Characterization and release characteristics of NPs. (A) Representative TEM images and EDX images of GA, BG NPs and MBG NPs (scale = 200 nm or 50 nm). (B) Drug release profile of gambogic acid from MBG NPs at pH 7.4. Error bars represent the mean ± SEM from three independent experiments (n = 3). (C) Representative particle size distribution curves (z-ave) of MnO_2, MB, BG and MBG NPs. Representative size images of MBG NPs. Error bars represent the mean ± SEM from three measurements (n = 3). (D) Zeta potential of MnO_2, MB, BG and MBG NPs. Error bars represent the mean ± SEM from three measurements (n = 3). (E) Size and PDI of BG NPs and MBG NPs in PBS over one week to demonstrate their stability. (F) Encapsulation efficiency of GA at different feed ratios. Error bars represent the mean ± SEM from three measurements (n = 3).

efficiency, we investigated the encapsulation efficiency under different feeding ratios. As shown in Fig. 2F, we found that as the MB ratio increased, the encapsulation efficiency improved, reaching a maximum of 76.86 ± 0.61% when the ratio of MB to GA was 15 : 4, indicating good loading capacity. This specific drug loading condition was selected for subsequent experiments.

2.2 NPs demonstrated initial burst GA release with dose-dependent cytotoxicity in CT26 cells and good biocompatibility

We studied the release profile of GA from the NPs over seven days (Fig. 2B). The results showed an initial burst release of GA, with nearly 50% of the loaded GA released within 72 hours. The release rate slowed in the following days, and approximately 60% of the loaded GA was released from the NPs within one week. Overall, the NPs supported a sustained release of GA for at least one week. Cell viability was measured using the CCK-8 assay. As shown in Fig. 3A, MBG NPs exhibited strong dose-dependent cytotoxicity against CT26 cells, with effective killing observed at concentrations above 0.4 μg mL^{-1}. Additionally, the MBG NPs demonstrated significantly greater cytotoxicity compared to the BG NPs. However, for NCM460 cells, neither the BG nor the MBG NPs exhibited noticeable cytotoxicity in the concentration, with cell viability remaining above 60% at 0.6 μg mL^{-1}. All these indicated

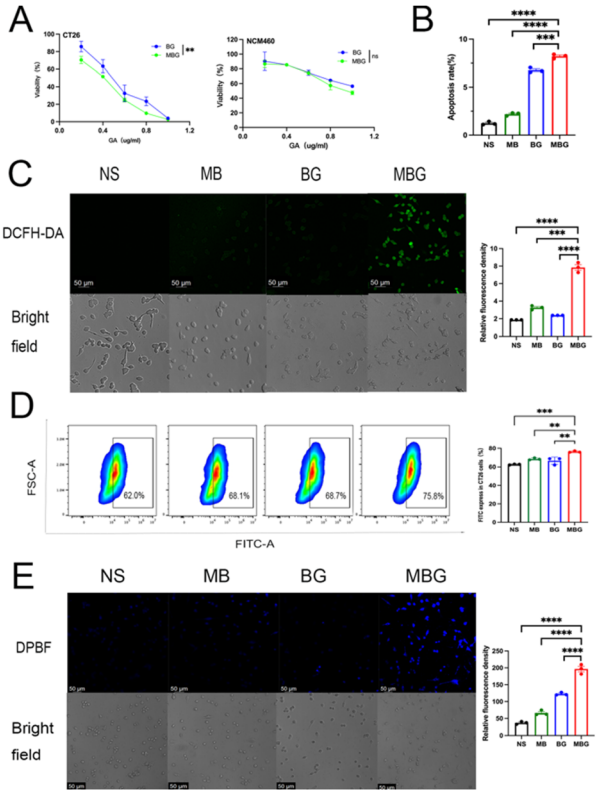

Fig. 3 *In vitro* antitumor efficacy of NPs. (A) CT26 and NCM460 cells were incubated for 24 hours with GA concentrations ranging from 0.2 μg ml^{-1} to a maximum of 1 μg ml^{-1}. The CCK8 reagent was added at specified time points, and the optical density change at 450 nm was measured. Error bars represent mean ± SEM (n = 3). P-values were calculated using paired Student's t-test. ** indicates p < 0.01, ns indicates P > 0.05. (B) Flow cytometric analysis of CT26 cells treated with NS, MB NPs, BG NPs, and MBG NPs after 12 hours of incubation using Annexin V-FITC and PI double staining. Error bars represent mean ± SEM (n = 3). P-values were calculated using one-way ANOVA and Tukey's multiple comparisons test; *** indicates P < 0.001, **** indicates P < 0.0001. (C) Monitoring of ROS using DCFH-DA as a probe after treatment of CT26 cells with NS, MB NPs, BG NPs, and MBG NPs for 2 hours, shown in confocal laser scanning microscopy (CLSM) images (scale = 50 μm). Fluorescence density results are shown on the far left. Error bars represent mean ± SEM (n = 3). P-values were calculated using one-way ANOVA and Tukey's multiple comparisons test; *** indicates P < 0.001, **** indicates P < 0.0001. (D) FCM patterns of DCFH-DA stained CT26 cells after various treatments. Error bars represent mean ± SEM (n = 3). P-values were calculated using one-way ANOVA and Tukey's multiple comparisons test; ** indicates P < 0.01, *** indicates P < 0.001. (E) Monitoring of $^1O_2$ using DPBF as a probe after treatment of CT26 cells with NS, MB NPs, BG NPs, and MBG NPs for 2 hours, shown in confocal laser scanning microscopy (CLSM) images (scale = 50 μm). Fluorescence density results are shown on the far left. Error bars represent mean ± SEM (n =3). P-values were calculated using one-way ANOVA and Tukey's multiple comparisons test; **** indicates P < 0.0001.

that the NPs have good biocompatibility. Using an apoptosis kit, we assessed drug-induced late-stage apoptosis. FCM results (Fig. 3B) indicated no significant cytotoxicity in the NS, MB NPs, whereas both the BG and MBG NPs showed cell killing effects, with the MBG NPs being more pronounced, further confirming the enhanced *in vitro* anti-tumor activity of our NPs.

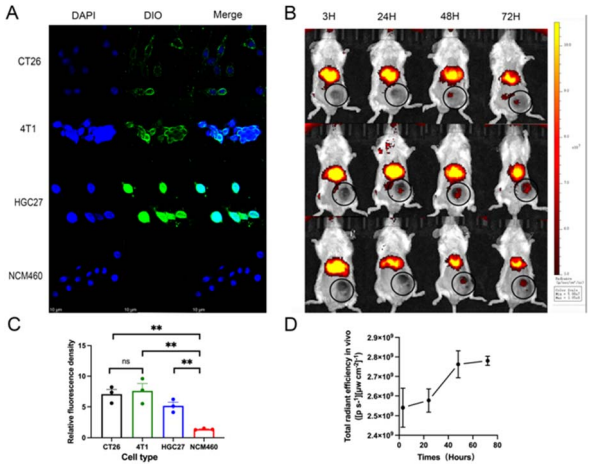

Fig. 4 *In vitro* uptake and *in vivo* biodistribution of NPs. (A) Confocal images of various cancer cells co-cultured with MBG NPs for 2 hours. NPs were labeled with DIO, and cell nuclei were stained with DAPI (scale = 10 μm). (B) Representative NIR imaging of CT26 tumor-bearing mice at designated times after intravenous injection of MBG NPs, with tumors circled for identification. NPs were stained with DIR prior to injection. The *Y* axis represents the total radiant efficiency *in vivo* ($[p\ s^{-1}][\mu w\ cm^{-2}]^{-1}$) ($n = 3$). (C) DIO relative fluorescence density results. Error bars represent mean ± SEM ($n = 3$). *P*-values were calculated using one-way ANOVA and Tukey's multiple comparisons test; ** indicates $p < 0.01$, ns indicates $P > 0.05$. (D) The change of fluorescence intensity at tumor site with time. The *Y* axis means the total radiant efficiency *in vivo* ($[p\ s^{-1}][\mu w\ cm^{-2}]^{-1}$) ($n = 3$).

2.3 MBG NPs preferentially targeted tumor cells, increasing ROS and $^1O_2$ levels and enhancing anti-tumor effects

To evaluate drug cellular uptake, we incubated various cell lines with DIO-labeled NPs. As shown in Fig. 4A and C, CT26, 4T1, and HGC27 cells showed green fluorescence (MB/DIO) clearly surrounding the blue nuclei (nuclei labeled with DAPI dye) and even overlapping each other. However, NCM460 cells showed significantly lower fluorescence intensity than other cells during the same incubation time. Fig. 4C showed the quantitative results of relative fluorescence density, and found that the relative fluorescence densities of CT26 and 4T1 were not statistically significant, while the fluorescence intensity of NCM460 was was indeed low. This observation showed that the drugs encapsulated within the NPs can preferentially target tumor cells, enhancing their anti-tumor efficacy.

The biodistribution of MBG NPs was detected by Near-infrared (NIR) fluorescence imaging (Fig. 4B and D), it was found that 24 hours after intravenous injection of the nanoparticles, red fluorescence began to appear at the tumor site. At 48 hours, a strong red fluorescence was detected and continued for 72 hours. This represents targeted enrichment of drugs in tumor and tumor-draining lymph nodes (TDLN), and recommends 24–48 hours after injection as the optimal treatment period.

Studies have shown that ROS can induce oxidative stress, which may lead to lipid peroxidation, protein damage, and DNA fragmentation.[23] We utilized DCFH-DA probes to indicate ROS levels in CT26 cells, observed through confocal microscopy and FCM. As expected, MBG NPs greatly increased the ROS levels in

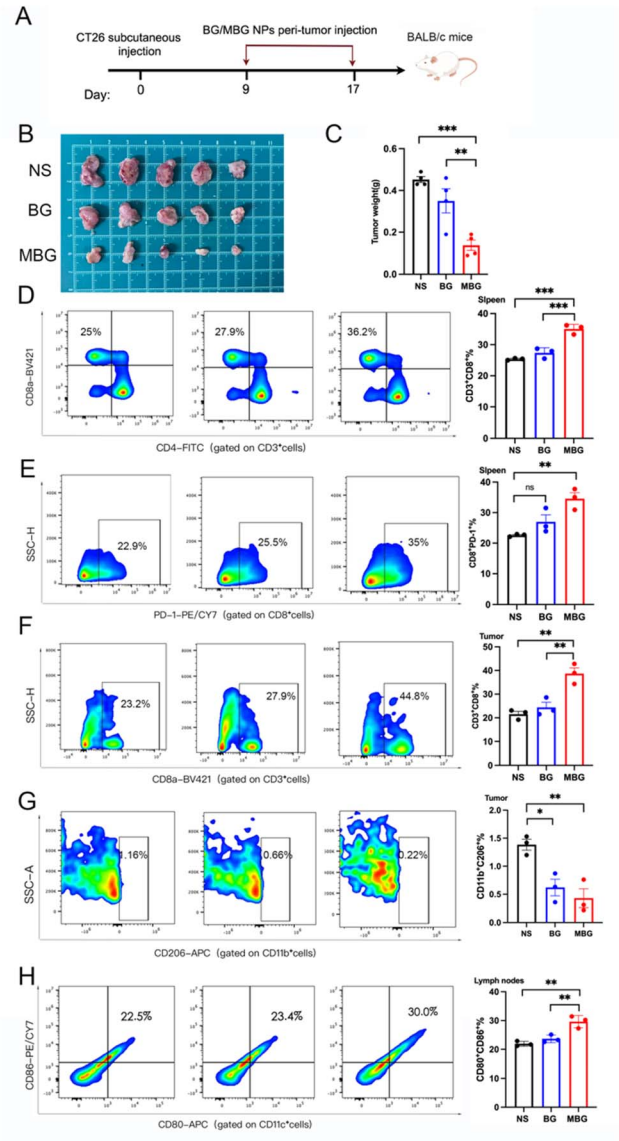

Fig. 5 Antitumor effects and induced immune response of NPs in subcutaneous models. (A) Schematic diagram of MBG NPs treatment in CT26 colon cancer-bearing mouse models. A suspension of 1×10^6 cells in 100 μl saline was subcutaneously injected into the right lower abdomen to establish the CT26 tumor model. Mice received subcutaneous injections of NS, BG NPs, or MBG NPs starting from day 9 post-inoculation, with a final volume of 100 μl per dose. GA concentration was set at 4 mg kg^{-1}. Weight and tumor diameter were measured every 2–3 days, and mice were euthanized three days after the final administration for flow cytometric staining and analysis of immune cell ratios in tumors, TDLNs, and spleens ($n = 5$). (B) Tumor images obtained from CT26-bearing BALB/c mice three days after the final administration ($n = 5$). (C) Tumor weights from different groups ($n = 5$). Flow cytometric analysis of $CD3^+CD8^+$ T cells (D), PD-1^+CD8^+ T cells (E) in spleens, $CD3^+CD8^+$ T cells (F), $CD11b^+CD206^+$ TAMs (M2 TAMs) (G) in tumors, and $CD80^+CD86^+$ mDCs (H) in TDLNs, with representative FCM images. Error bars represent mean ± SEM ($n = 3$). *P*-values were calculated using one-way ANOVA and Tukey's multiple comparisons test; ns indicates $P > 0.05$, * indicates $P < 0.05$, ** indicates $P < 0.01$, *** indicates $P < 0.001$.

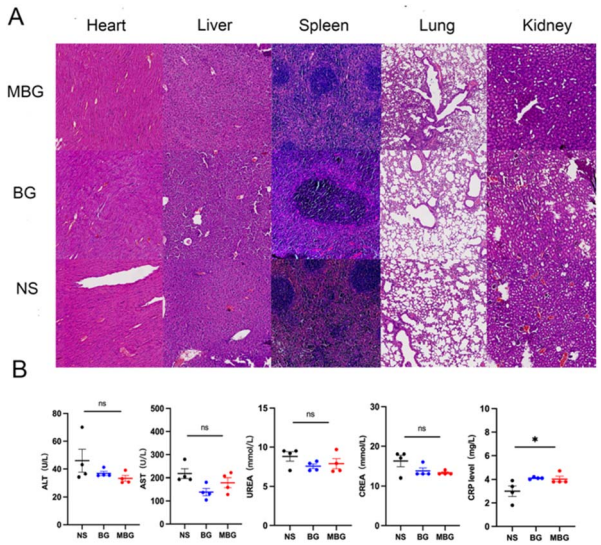

Fig. 6 Evaluation of biosafety of NPs post-administration in mice. (A) H&E staining images of heart, liver, spleen, lung, and kidney in CT26 tumor-bearing mice models from MBG, BG, and NS groups three days after the last treatment (scale = 200 μm). (B) Blood biochemistry and hematological data of BALB/c mice three days after the last treatment ($n = 4$). Error bars represent mean ± SEM. *P*-values were calculated using one-way ANOVA and Tukey's multiple comparisons test; ns indicates $P > 0.05$, * indicates $P < 0.05$.

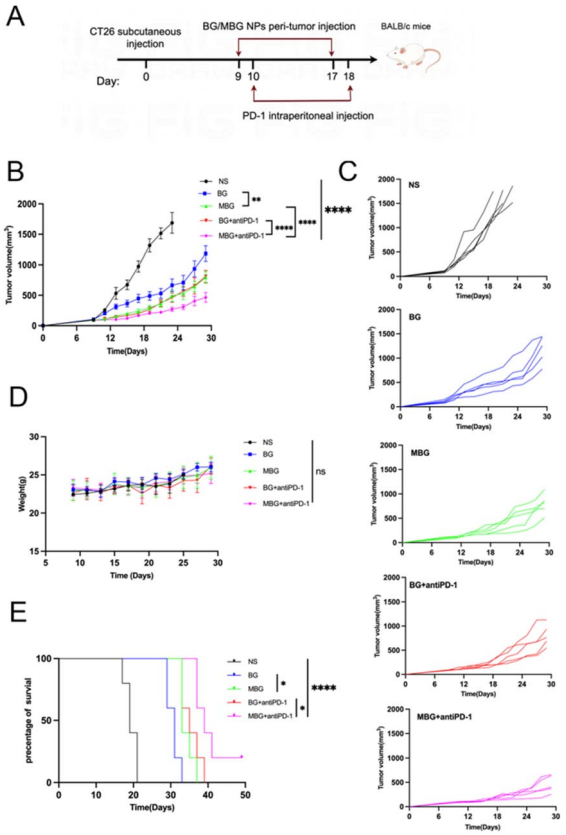

Fig. 7 Synergistic antitumor effects of NPs and aPD-1 in subcutaneous models. (A) Schematic diagram of the administration of NPs and aPD-1 in CT26 tumor-bearing mice. 1×10^6 CT26 cells were inoculated subcutaneously in the right lower abdomen to establish the CT26 tumor model. Starting from day 9 post-inoculation, NPs were injected subcutaneously, and aPD-1 was injected intraperitoneally, with tumor size and mouse weight measured every 2–3 days until survival endpoints. (B) Average tumor growth curves of BALB/c mice bearing CT26 tumors under different treatments (NS, BG, MBG, BG + aPD-1, MBG + aPD-1), with tumor sizes measured every 2–3 days. Error bars represent mean ± SEM ($n = 5$). *P*-values were calculated using two-way ANOVA and Tukey's multiple comparisons test; ns indicates $P > 0.05$, * indicates $P < 0.05$, ** indicates $P < 0.01$, *** indicates $P < 0.001$, **** indicates $P < 0.0001$. (C) Tumor growth curves for individual mice over 30 days in different groups ($n = 5$). (D) Average body weight of mice in different groups over 30 days, with error bars representing mean ± SEM ($n = 5$). *P*-values were calculated using unpaired Student's *t*-test; ns indicates $P > 0.05$. (E) Survival curves of different groups over 50 days, with error bars representing mean ± SEM ($n = 5$). *P*-values were calculated using log-rank test; * indicates $P < 0.05$, **** indicates $P < 0.0001$.

CT26 cells, reversed the hypoxic acidic TME. Confocal microscopy showed the fluorescence intensity in the MBG NPs was significantly stronger than that of the MnO_2 or GA monotherapy groups (Fig. 3C). FCM (Fig. 3D) reflected a gradual increase in the percentage of ROS-positive cells, peaking after treatment with MBG NPs. Singlet oxygen($^1O_2$)is one of the radicals that can participate in the non-specific reactions that lead to the destruction of cells.[24] It was shown by Fig. 3E, MBG NPs also induced CT26 cells to produce a higher concentration of $^1O_2$.

2.4 MBG NPs inhibited tumor growth *in vivo*, increased $CD8^+$ T cell infiltration, reduced M2-type macrophages, and promoted anti-tumor immunity

To evaluate the anti-tumor effects of MBG NPs *in vivo*, we established a subcutaneous CT26 colon cancer model in male BALB/c mice and administered treatment *via* peritumoral injection at specified time points (Fig. 5A). Three days after the last administration, mice were euthanized. As shown in Fig. 5B and C, tumors in the MBG NPs showed significant growth inhibition, with tumor weights and volumes consistent. Tumors, spleens, and TDLNs were then excised for FCM analysis. Fig. 5D and E showed that the percentage of $CD3^+CD8^+$ T cells in the spleens of the MBG NPs (36.2%) was significantly higher than that in the NS (25%) and BG groups (27.8%), with increased programmed death-1 (PD-1) expression on $CD8^+$ T cells. In tumors, the MBG NPs also showed nearly double the percentage of $CD3^+CD8^+$ T cells (44.8%) compared to the NS group (23.2%) (Fig. 5F). In this study, we found that MBG NPs could reverse hypoxia and increase the expression of $CD8^+$ T cells. Previous studies have shown that improving hypoxia can promote M2-to-M1 polarization of TAMs.[25] So, we investigated the expression of tumor-associated macrophages (TAMs) in tumor tissues, type macrophages ($CD11b^+CD206^+$) in the MBG NPs compared to controls (Fig. 5G). Furthermore, the MBG NPs increased mature DCs in TDLNs (Fig. 5H). In conclusion, MBG NPs release high ROS levels, regulate the TME, reduce hypoxia, enhance anti-tumor immunity, and promote immune-mediated tumor killing by transforming "cold tumors" into "hot tumors".

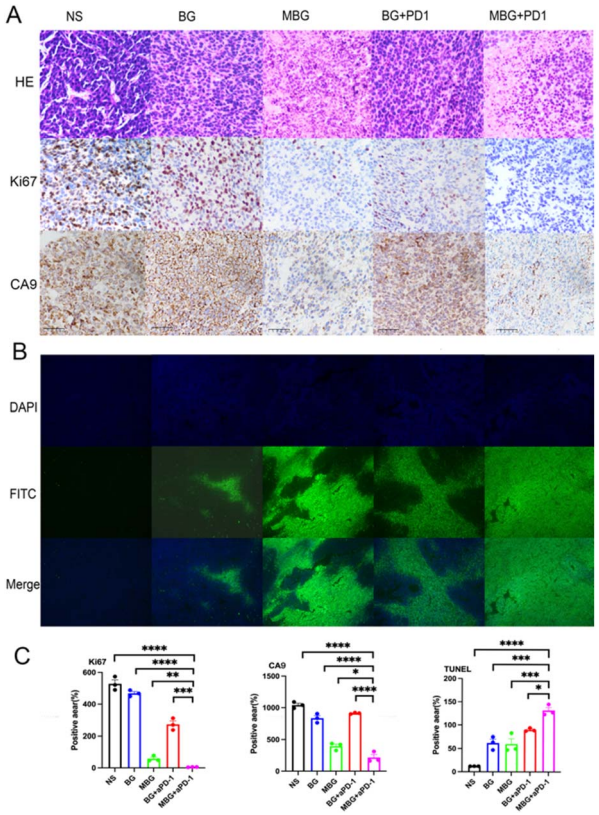

Fig. 8 Representative immunohistochemical and immunofluorescence images of tumors post-administration. (A) H&E and immunohistochemical sections of tumors. Upper panel: H&E-stained sections of tumors from different groups; middle panel: Ki67 staining of tumor tissues; lower panel: CA9 staining of tumor tissues (scale = 50 μm). (B) Representative images of TUNEL immunofluorescence staining of tumor sections (scale = 100 μm). (C) Positive area quantitative results of Ki67, CA9 and TUNEL. Error bars represent mean ± SEM. *P*-values were calculated using one-way ANOVA and Tukey's multiple comparisons test; * indicates $P < 0.05$, ** indicates $P < 0.01$, *** indicates $P < 0.001$, **** indicates $P < 0.0001$.

2.5 MBG NPs showed optimal tumor accumulation 24–48 hours post-injection, with no significant systemic toxicity or organ damage

We assessed the biodistribution of MB/DIR NPs using IVIS Lumina III system (Fig. 4B), as high accumulation of NPs in tumors is crucial for achieving favorable therapeutic outcomes. Forty-eight hours post intravenous injection, we detected strong red fluorescence in the tumor region of CT26 tumor-bearing mice, which persisted up to 72 hours, while NPs in the liver were gradually eliminated after 48 hours. These results indicate the fluorescence detectability of NPs and suggest that 24–48 hours post-injection is the optimal treatment window.

In mice treated with different NPs, we histologically evaluated the systemic toxicity of BG NPs and MBG NPs by assessing major organs (heart, liver, spleen, lung, and kidney) with H&E staining (Fig. 6A). No significant histological differences were observed between the NS and BG, MBG NPs, and no obvious signs of inflammatory response were detected in these critical organs. Additionally, serum biochemical assays (Fig. 6B) showed no significant differences in serum biochemical markers among groups, the C-reactive protein (CRP) level in the MBG NPs was slightly elevated but remained within the normal range. These findings indicate that MBG NPs possess good biocompatibility and safety *in vivo*.

2.6 MBG NPs enhanced aPD-1 immunotherapy

The hypoxic TME,[26] insufficient T cell activation and infiltration[27] and other factors, limit the benefit that patients can gain from ICIs. Our previous studies confirmed that GA synergizes with aPD-1 to achieve better anti-tumor effects,[7] but the exact reason remains unclear. Prior reports have suggested that acidic tumor microenvironment with hypoxia can induce high programmed cell death ligand-1 (PD-L1) expression, leading to immune escape in tumors.[28–30] Mn^{2+} can improve hypoxic and acidic environment, disrupt the PD-1/PD-L1 axis, and reverse the immunosuppressive microenvironment.[9] Mn^{2+} combined with ICIs can enhance antitumor efficacy while reducing the required dose of aPD-1 in mice.[31] So, we established a mouse xenograft tumor model using CT26 cells to verify this. Tumor-bearing mice were randomly divided into five groups ($n = 5$) and treated with NS, BG, MBG, BG + aPD-1, and MBG + aPD-1, monitoring tumor volume and body weight every 2–3 days until the endpoint (Fig. 7A). As shown in Fig. 7B, the tumors in mice injected with NS or BG NPs grew rapidly. However, the addition of MnO_2 enhanced the anti-tumor efficacy, and the MBG + aPD-1 group demonstrated the most remarkable tumor inhibitory effect. Fig. 7C displayed tumor growth over 30 days, with nearly two-thirds of mice in the MBG + aPD-1 group showing slow tumor growth, maintaining volumes below 500 mm^3. Body weight monitoring revealed no significant differences among groups (Fig. 7D). The mice in the NS group survived for an average of 20 days. Those in the BG, MBG, and BG + aPD-1 groups survived for 30–35 days. Meanwhile, the MBG + aPD-1 group survived for a significantly longer period (Fig. 7E). Our results suggest that the combination of MBG NPs and aPD-1 provided the best overall antitumor effect, significantly prolonged mouse survival.

2.7 Immunohistochemistry and immunofluorescence staining showed MBG NPs change TME

CA9 is a membrane-associated zinc metalloenzyme that enables tumor cells to survive in hypoxic acidic environments.[30] It also has been reported that hypoxia and acidity contribute to tumor resistance.[29] In the H&E-stained sections (Fig. 8A), we observed a general trend of decreased cellular density in tumors treated with MBG NPs. In staining for CA9, the levels significantly decreased in tumors treated with Mn^{2+} NPs, supporting our earlier investigation into the targeted effects of this material on tumors. We also noted significantly ki67 lower expression levels in the MBG NPs, alongside an increase in TUNEL expression (Fig. 8B), which was more pronounced in the MBG NPs combined with aPD-1. The quantitative results of positive area in Fig. 8C also prove this conclusion. These results suggested that MBG NPs treatment recruited more T cells to activate systemic antitumor immunity and reduced the expression of CA9 and the resistance of drug.

That may explain why it has a better synergistic effect with aPD-1. Collectively, the experiments confirm that MBG NPs, by promoting ROS generation, have the potential to remodel the TME, potentially enhancing the efficacy of immunotherapy by alleviating hypoxia-induced acid environment and aPD-1 resistance.

3. Materials and methods

3.1 Materials

The reagents used in this study were as follows: gambogic acid (purity ≥98%) purchased from Source Leaf Biotechnology (Shanghai, China); manganese chloride ($MnCl_2$) purchased from Mcklin (Shanghai, China); tetramethylammonium hydroxide (TMA·OH, 25% wt) purchased from Aladdin (Shanghai, China); bovine serum albumin (BSA, purity ≥97%) purchased from Pusitang Biotechnology (Beijing, China); hydrogen peroxide (H_2O_2, 30% wt) purchased from Sigma (USA); annexin V-FITC/PI apoptosis kit purchased from LinkBio (Hangzhou, China); reactive oxygen species assay kit (including 2,7-dichlorofluorescein diacetate (DCFH-DA)) purchased from Biyuntian Biotechnology (Shanghai, China); 1,3-diphenylbenzofuran (DPBF) purchased from MedChemExpress (USA) and mouse antibodies including CD3, CD4, CD8a, programmed death-1 antibodies (PD-1), CD11c, CD80, CD86, CD11b, and CD206, all purchased from Biolegend (USA).

3.1.1 Cells. CT26 (mouse colon cancer cells) and NCM460 (human normal intestinal epithelial cells) were obtained from the American Type Culture Collection (ATCC). Cells were cultured in RPMI-1640 medium (Gibco Inc., New York, USA) supplemented with 10% fetal bovine serum (Gibco Inc., New York, USA) and 1% penicillin–streptomycin solution (Beyotime Biotechnology Company, Shanghai, China). Cells were incubated at 37 °C in a cell culture incubator with 5% CO_2.

3.1.2 Animals. Male BALB/c mice, 6 weeks old, were purchased from Shanghai Sippr-Bik Biotechnology Co., Ltd. (Shanghai, China). All mice were kept in the specific pathogen-free (SPF) laboratory animal center of Nanjing Drum Tower Hospital (Nanjing, China). All animal experiments were approved by the Animal Management and Use Committee of Nanjing Drum Tower Hospital (2024AE01034).

3.2 Preparation and characterization of MBG NPs

3.2.1 Preparation of MBG NPs. MnO_2 nanosheets were prepared using $MnCl_2$, TMA·OH, and H_2O_2 as raw materials.[32] A 10 mL solution of 0.3 M $MnCl_2$ was added to 20 mL of a mixture (0.6 M TMA·OH and 30 wt% H_2O_2), resulting in a deep brown solution. The solution was vigorously stirred on a shaker at 25 °C for 12 hours, then centrifuged at 10 000 rpm for 10 minutes. The precipitate was collected and washed three times with methanol and ultrapure water. Subsequently, the precipitate was freeze-dried using a vacuum freeze dryer. Under ultrasonic agitation(950 W, 25 kHz for 8 h in an ice-bath),[21] 15 mg of BSA was added to 1 mg of the dispersed MnO_2 nanosheet system and reacted for 8 hours to obtain the MnO_2-BSA (MB) carrier, which was stored at 4 °C. In this study, the Nab™ technique was used to prepare GA NPs: the aqueous phase was an BSA solution, and the oil phase was a mixed solution of dichloromethane and ethanol dissolving GA. The oil phase was transferred to the aqueous phase, uniformly emulsified by ultrasound, and then the organic solvent was removed by rotary evaporation. The solution was filtered through a 0.45 μm filter membrane to remove potential Garcinia precipitate, yielding MBG NPs for later use.

3.2.2 Characterization of MBG NPs. The particle size and zeta potential of MnO_2, MB, BG, and MBG NPs were measured using a dynamic light scattering (DLS) analyzer (Zetasizer, Malvern, UK). The size and dispersion were also measured *via* DLS over a 7 days period. The morphology of GA, BG NPs, MBG NPs were characterized using transmission electron microscopy (TEM), and the composition of the elements was verified by scattering X-ray spectroscopy(EDX). The encapsulation efficiency of GA in MBG NPs was determined by high-performance liquid chromatography (HPLC) (Shimadzu, Japan).

3.2.3 *In vitro* GA release. For *in vitro* release studies, 1 mL of MBG NPs was transferred into a pre-swollen dialysis bag (MWCO: 12–14 kDa). The bag was immersed in 1 mL of phosphate buffered saline (PBS, pH 7.4) containing 0.5% Tween 80 and incubated in a shaking incubator at 37 °C. Three parallel experiments were set up. At predetermined time points (0, 1, 3, 5, 7, 9, 24, 72, 120, 168 hours), 500 μL of the release medium was withdrawn and replaced with fresh medium. All samples were analyzed using HPLC.

3.3 *In vitro* cell studies

3.3.1 *In vitro* cytotoxicity. The *in vitro* cytotoxicity of different formulations was assessed using a Cell Counting Kit-8 (CCK-8). CT26 or NCM460 cells were seeded in 96-well plates (3000 cells per well in 100 μL medium) and cultured for 24 hours. Afterward, the cells were treated with 1640 medium containing BG or MBG NPs, where the final concentration of GA ranged from 0.2 to 1 μg mL^{-1}. After 24 hours of incubation, CCK-8 solution was added to each well. The optical density (OD) was measured at 450 nm using a microplate reader (Thermo Fisher, USA).

3.3.2 Apoptosis assay. CT26 cells were seeded in 6-well plates (1.5×10^5 cells per well in 1 mL medium) and cultured for 24 hours. Cells were then treated with BG and MBG NPs with a final GA concentration of 0.4 μg mL^{-1}. After 12 hours of incubation, the cells were collected, stained with an apoptosis detection kit, and analyzed using flow cytometry (FCM, CytoFLEX, Beckman, USA).

3.3.3 ROS measurement. CT26 cells were seeded in confocal culture dishes (1.5×10^5 cells per well in 1 mL medium) and cultured for 24 hours. After incubation with MB, BG, or MBG NPs for 2 hours, cells incubated with serum-free medium containing 0.1 mM 2′,7′-dichlorodihydrofluorescein diacetate (DCFH-DA) in the dark at 37 °C for 30 minutes. The images were captured using a confocal laser scanning microscope (Leica, Germany).

In a separate experiment, CT26 cells that have been treated differently were then resuspended in 1 mL of serum-free medium and stained with 0.1 mM DCFH-DA at 37 °C in the dark for 30 minutes. Fluorescence was measured using FCM,

and ROS levels were determined from the fluorescence intensity.

3.3.4 $^1O_2$ measurement. The ability of cells to produce $^1O_2$ under MBG NPs stimulation was verified with 1,3-diphenylbenzofuran (DPBF). CT26 cells were inoculated in confocal culture dishes and cultured for 24 hours. After incubating with MB, BG or MBG NPs for 2 hours, incubate with DPBF in 37 °C darkness for 30 minutes. The images were captured using confocal laser scanning microscope (Leica, Germany).

3.3.5 *In vitro* cellular uptake. Cellular uptake was evaluated using CT26, 4T1 (mouse breast cancer), HCG27 (human gastric cancer), and NCM460 cells. Cells were seeded in confocal culture dishes and incubated overnight, then were incubated with MB/DIO for 2 hours and stained with 4′,6-diamidino-2-phenylindole (DAPI) to label the nuclei. Cellular uptake was visualized using confocal laser scanning microscopy. MB/DIO NPs were prepared by loading MB with DIO dye.

3.4 Biodistribution study

CT26 cells (1×10^6) were subcutaneously injected into the right flank of BALB/c mice. One week later, MB/DIR was intravenously injected into the mice. The mice were anesthetized with isoflurane and imaged at 3, 24, 48, and 72 hours using near-infrared fluorescence imaging system (IVIS Lumina III system) (PerkinElmer, USA). The average fluorescence intensity was analyzed using region of interest (ROI) selection. MB/DIR NPs were prepared by loading MB with DIR dye.

3.5 *In vivo* experiments

3.5.1 Analysis of antitumor immune responses. CT26 cells (1×10^6) were inoculated subcutaneously into the right flank of 6 week-old male BALB/c mice to establish a colon cancer burden model. When the tumor volume reached approximately 100 mm^3, the mice were randomly divided into three groups ($n = 5$) to ensure similar average tumor volumes. On the 9th and 17th days after post-tumor implantation, different formulations were administered around the tumor: NS (control group), BG NPs, and MBG NPs (GA, 4 mg kg^{-1}, peritumoral injection). Animal body weight and tumor volume were measured every 2 or 3 days until the end of the experiment. Tumor volume (V) was calculated using the formula: $V = (L \times W \times W)/2$ (where L is the longest diameter of the tumor and W is the shortest diameter perpendicular to the length). Mice were sacrificed 3 days after the last administration ($n = 3$), and fresh spleen, tumor, and tumor-draining lymph nodes (TDLNs) were collected for FCM. All samples were stained with specific antibodies for 30 minutes in the dark at 4 °C and then washed. FCM was performed to collect data, which were analyzed using FlowJo X (FlowJo). The monoclonal antibodies (mAbs) used in FCM included: CD3-APC, CD4-FITC, CD8a-BV421, PD-1-PE/CY7, CD11c-PE, CD80-APC, CD86-PE/CY7, CD11b-BV510, and CD206-APC (Biolegend, USA)

3.5.2 *In vivo* antitumor activity. To evaluate the *in vivo* antitumor efficacy of the NPs and their combination with aPD-1 immunotherapy, 1×10^6 CT26 cells were subcutaneously inoculated into BALB/c mice. Once the tumor volume reached approximately 100 mm^3, the mice were randomly divided into five groups ($n = 3$). On the 9th and 17th days after post-tumor implantation, the mice received the following peritumoral injections: NS, BG, MBG, BG combined with aPD-1, and MBG combined with aPD-1 (GA, 4 mg kg^{-1}, peritumoral injection; aPD-1, 100 μg each, intraperitoneal injection). The body weight and tumor volume were measured every 2 or 3 days. Long-term survival analysis was conducted, and the mice were sacrificed when the tumor volume reached 1500 mm^3.

3.5.3 Safety evaluation. After euthanizing the mice, tumor tissue and major organs (heart, lungs, liver, spleen, and kidneys) from each group were collected for hematoxylin and eosin (H&E). Blood samples were also collected for biochemical analysis. Systemic toxicity was assessed by blood biochemistry and H&E staining of organ sections.

3.5.4 Immunohistochemical staining. Tumor samples from BALB/c mice were fixed using a 4% formaldehyde solution and subsequently embedded in paraffin. The formalin-fixed, paraffin-embedded tissue specimens were sectioned into 5 μm slices and incubated overnight at 4 °C with primary antibodies proliferation-associated antigen-67 (Ki67, CST-9129, 1:200) and carbonic anhydrase IX (CA9, CST, 11071-1-1-AP 1:500). Following this, the sections were incubated at room temperature for 1 hour with horseradish peroxidase (HRP)-labeled secondary antibodies. The samples were then stained using 3,3′-diaminobenzidine (DAB) and hematoxylin. The staining intensity was assessed independently by two experienced pathologists.

3.5.5 Immunofluorescence staining. Multiple immunofluorescence (mIF) was performed on a series of 5.0 μm histological tumor sections from all samples using transferase-mediated dideoxy uridine triphosphate-biotin nick end labeling (TUNEL) BrightGreen Apoptosis Detection Kit (Vazyme, China). The antibody staining procedure was standardized across all sections. Sections were subsequently back stained with DAPI for visualization.

3.6 Statistical analysis

Statistical analysis was performed using GraphPad Prism software (version 9.0). Fluorescence and immunohistochemistry density was performed using Image J software. All experiments were repeated at least three times. Data are expressed as mean ± standard error of the mean (SEM). An unpaired one-tailed Student's t-test was used to compare two groups, and a one-way analysis of variance (ANOVA) with Tukey's post-hoc test was employed to compare more than two groups. Survival analysis was conducted using Kaplan–Meier estimates with log-rank tests. Statistical significance was defined as: $^*p < 0.05$, $^{**}p < 0.01$, $^{***}p < 0.001$, and $^{****}p < 0.0001$. Graphs were generated using Adobe Photoshop 2021.

4. Conclusions

In summary, we first combined MnO_2 and GA, both of which target acid environment and improve hypoxia, using BSA as a compatible delivery method for GA, achieving a synergistic effect in enhancing the killing of tumor cells and improving tumor cell resistance. This particle enhances T cell expression

in tumor regions and effectively improves the efficacy of aPD-1 treatment for MSS CRC. Moreover, the particle exhibits excellent biocompatibility, ensuring precise targeting without causing severe toxic side effects in the host. However, due to laboratory limitations, we currently cannot explore molecular pathways in depth, nor have we fully investigated optimal concentration ratios. In future research, we will delve into the specific molecular regulatory mechanisms in CRC and the optimal concentration ratios of Mn^{2+}, GA, and BSA to achieve more precise targeting and treatment. Overall, this study offers a combined therapeutic strategy that enhances tumor killing while alleviating hypoxia and improving the efficacy of ICIs. We hope this research will have a positive impact in the era of precision cancer treatment.

Ethical statement

All animal experiments were approved by the Laboratory Animal Care and Use Committee of the Affiliated Nanjing Drum Tower Hospital of Nanjing University Medical School (Checking number: 2024AE01034), and were carried out in compliance with all relevant ethical regulations.

Data availability

All the data supporting this article have been included in the research article. If the raw data is required, it will be made available on request.

Author contributions

Zixin Liang: writing – original draft, software, resources, project administration, methodology, investigation, formal analysis, data curation. Xinyi Xu: investigation, formal analysis. Ning wang: investigation. Xintao He: investigation. Xingzhi Han: investigation. Liuqi Sang: investigation. Jing Hu: writing – review & editing, conceptualization. Xiaoping Qian: writing – review & editing, funding acquisition.

Conflicts of interest

The authors declare no conflict of interest.

Acknowledgements

This study was supported by grants from Nanjing health science and technology development key program (no ZKX21028), Jiangsu scientific and technological development of traditional Chinese medicine Key projects (no ZD202227), provincial natural science foundation of Jiangsu (no BK20211007). Figure support was provided by Figdraw.

References

1 R. L. Siegel, A. N. Giaquinto and A. Jemal, *CA Cancer J. Clin.*, 2024, **74**, 12–49.
2 M. Fakih, J. Sandhu, D. Lim, X. Li, S. Li and C. Wang, *JAMA Oncol.*, 2023, **9**, 627–634.
3 S. Jiao, S. K. Subudhi, A. Aparicio, Z. Ge, B. Guan, Y. Miura and P. Sharma, *Cell*, 2019, **179**, 1177–1190.
4 E. Hatami, M. Jaggi, S. C. Chauhan and M. M. Yallapu, *Biochim. Biophys. Acta, Rev. Cancer*, 2020, **1874**, 188381.
5 Q. Zhang, Y. Zhang, C. Wang, H. Tang, A. Ma, P. Gao, Q. Shi, G. Wang, S. Shen, J. Zhang, F. Xia, Y. Zhu and J. Wang, *Phytomedicine*, 2024, **129**, 155657.
6 Z. Zhang, H. Qian, M. Yang, R. Li, J. Hu, L. Li, L. Yu, B. Liu and X. Qian, *Int. J. Nanomed.*, 2017, **12**, 1593–1605.
7 F. Huang, Q. Zhang, J. Xiao, X. Zhang, X. Han, X. Shi, J. Hu, L. Li and X. Qian, *Int. J. Nanomed.*, 2023, **18**, 2261–2273.
8 Z. Z. Lim, J. E. Li, C. T. Ng, L. Y. Yung and B. H. Bay, *Acta Pharmacol. Sin.*, 2011, **32**, 983–990.
9 B. Ding, J. Yue, P. Zheng, P. Ma and J. Lin, *J. Mater. Chem. B*, 2021, **9**, 7117–7131.
10 L. Hou, C. Tian, Y. Yan, L. Zhang, H. Zhang and Z. Zhang, *ACS Nano*, 2020, **14**, 3927–3940.
11 T. Song, Y. Liao, Q. Zuo, N. Liu and Z. Liu, *J. Mater. Chem. B*, 2022, **10**, 3474–3490.
12 J. Y. Hong, Y. G. Lim, Y. J. Song and K. Park, *Int. J. Biol. Macromol.*, 2023, **226**, 121–131.
13 Y. Jing, C. Wang, C. Li, Z. Wei, D. Lei, A. Chen, X. Li, X. He, L. Cen, M. Sun, B. Liu, B. Xue and R. Li, *Int. J. Biol. Macromol.*, 2024, **270**, 132348.
14 Z. Geng, F. Chen, X. Wang, L. Wang, Y. Pang and J. Liu, *Biomaterials*, 2021, **275**, 120897.
15 S. S. Ahmed, M. Z. Baba, U. Wahedi, J. Koppula, M. V. Reddy, D. Selvaraj, S. Venkatachalam, J. Selvaraj, V. Sankar and J. Natarajan, *Int. J. Biol. Macromol.*, 2024, **279**, 135487.
16 C. Weekes and V. Narayanan, *Gastrointest. Cancer: Targets Ther.*, 2015, 11.
17 Y. Gan, N. Hu, C. He, S. Zhou, J. Tu, T. Liang, Y. Pan, D. Kirsanov, A. Legin, H. Wan and P. Wang, *Biosens. Bioelectron.*, 2019, **130**, 254–261.
18 B. Xiao, X. Zhou, H. Xu, B. Wu, D. Hu, H. Hu, K. Pu, Z. Zhou, X. Liu, J. Tang and Y. Shen, *ACS Nano*, 2018, **12**, 12682–12691.
19 L. Deng, T. Wei, Y. Zhang, A. Shen, X. He, S. Gao, X. Li, W. He, A. Haleem, R. Hu, H. Cheng and S. Chen, *Int. J. Pharm.*, 2024, **660**, 124303.
20 L. Han, Y. Wang, X. Huang, F. Liu, C. Ma, F. Feng, J. Zhang, W. Liu, W. Qu, H. Pang and J. Xue, *Biomaterials*, 2020, **257**, 120228.
21 W. Xiu, S. Gan, Q. Wen, Q. Qiu, S. Dai, H. Dong, Q. Li, L. Yuwen, L. Weng, Z. Teng, Y. Mou and L. Wang, *Research*, 2020, **2020**, 9426453.
22 G. Yang, L. Xu, Y. Chao, J. Xu, X. Sun, Y. Wu, R. Peng and Z. Liu, *Nat. Commun.*, 2017, **8**, 902.
23 D. Wang, W. Ma, Y. Zhang, Y. Wang, L. Sun, J. Jiang, L. Jiao, R. Li, Y. Zhang, M. Zhang and Q. Zhou, *Biomaterials*, 2025, **313**, 122778.
24 K. Malarz, W. Borzęcka, P. Ziola, A. Domiński, P. Rawicka, K. Bialik-Wąs, P. Kurcok, T. Torres and A. Mrozek-Wilczkiewicz, *Bioorg. Chem.*, 2025, **155**, 108127.

25 Y. Gong, W. Gao, J. Zhang, X. Dong, D. Zhu and G. Ma, *J. Nanobiotechnol.*, 2024, **22**, 341.
26 G. Luo, X. Li, J. Lin, G. Ge, J. Fang, W. Song, G. G. Xiao, B. Zhang, X. Peng, Y. Duo and B. Z. Tang, *ACS Nano*, 2023, **17**, 15449–15465.
27 J. M. Zaretsky, A. Garcia-Diaz, D. S. Shin, H. Escuin-Ordinas, W. Hugo, S. Hu-Lieskovan, D. Y. Torrejon, G. Abril-Rodriguez, S. Sandoval, L. Barthly, J. Saco, B. Homet Moreno, R. Mezzadra, B. Chmielowski, K. Ruchalski, I. P. Shintaku, P. J. Sanchez, C. Puig-Saus, G. Cherry, E. Seja, X. Kong, J. Pang, B. Berent-Maoz, B. Comin-Anduix, T. G. Graeber, P. C. Tumeh, T. N. Schumacher, R. S. Lo and A. Ribas, *N. Engl. J. Med.*, 2016, **375**, 819–829.
28 A. Akinleye and Z. Rasool, *J. Hematol. Oncol.*, 2019, **12**, 92.
29 C. B. Yang, H. X. Feng and C. L. Dai, *Cancer Med.*, 2022, **11**, 2329–2341.
30 A. W. Eckert, S. Horter, D. Bethmann, J. Kotrba, T. Kaune, S. Rot, M. Bache, U. Bilkenroth, W. Reich, T. Greither, C. Wickenhauser, D. Vordermark, H. Taubert and M. Kappler, *Int. J. Mol. Sci.*, 2019, **20**, 375.
31 M. Lv, M. Chen, R. Zhang, W. Zhang, C. Wang, Y. Zhang, X. Wei, Y. Guan, J. Liu, K. Feng, M. Jing, X. Wang, Y. C. Liu, Q. Mei, W. Han and Z. Jiang, *Cell Res.*, 2020, **30**, 966–979.
32 C. Chu, H. Lin, H. Liu, X. Wang, J. Wang, P. Zhang, H. Gao, C. Huang, Y. Zeng, Y. Tan, G. Liu and X. Chen, *Adv. Mater.*, 2017, **29**(23), 1–13.